Journal of *Marine Science and Engineering*

MDPI

Article

Influence of Marine Environmental Factors on Characteristics of Composite Magnetic Field of Underwater Vehicles

Honglei Wang [1,2], Xinyu Dong [1,2,*] and Yixin Yang [1,2]

[1] School of Marine Science and Technology, Northwestern Polytechnical University, Xi'an 710072, China; wanghonglei@nwpu.edu.cn (H.W.); yxyang@nwpu.edu.cn (Y.Y.)
[2] Shaanxi Key Laboratory of Underwater Information Technology, Xi'an 710072, China
* Correspondence: dxy18817563593@outlook.com

Abstract

This research study investigated the composite magnetic fields of underwater vehicles in the presence of ocean waves under varying conductivity, analyzed their spatiotemporal characteristics, attenuation laws, and influence mechanism. We integrated the modeling of three types of magnetic fields to obtain a composite magnetic field: the magnetic anomaly field generated by a ferromagnetic vehicle was simulated with a hybrid ellipsoid–dipole model, the wake magnetic field generated by its motion, and the ocean wave magnetic field generated by wind-driven waves were derived from the velocity fields. Simulation results show that the magnetic anomaly and wake magnetic fields are mainly influenced by vehicle speed, course, and diving depth, while the ocean wave magnetic field is affected by wind speed and direction. The composite magnetic field's intensity increases with vehicle and wind speed but decreases with the increase in diving depth. This study offers a comprehensive analysis of the composite magnetic fields of underwater vehicles in the presence of ocean waves, emphasizing the significant impact of vehicle motion and marine environmental parameters. These insights are essential to gaining a deeper understanding of the magnetic fields generated by underwater vehicles as they navigate ocean waves.

Keywords: underwater vehicle; magnetic anomaly; wake magnetic; ocean waves; composite magnetic field

Received: 28 August 2025
Revised: 17 September 2025
Accepted: 23 September 2025
Published: 24 September 2025

Citation: Wang, H.; Dong, X.; Yang, Y. Influence of Marine Environmental Factors on Characteristics of Composite Magnetic Field of Underwater Vehicles. *J. Mar. Sci. Eng.* **2025**, *13*, 1850. https://doi.org/10.3390/jmse13101850

1. Introduction

Given that underwater vehicles are increasingly quieter, traditional acoustic detection methods have become inadequate, driving the need for non-acoustic detection technologies [1]. Magnetic detection, which stands out as a promising alternative [2], is a method to detect and identify underwater vehicles sailing in the presence of ocean waves by utilizing the generated magnetic fields [3]. As shown in Figure 1, the magnetic fields measured by detectors can be primarily classified into three types based on their origin:

- The magnetic anomaly field generated by the magnetization of a vehicle's ferromagnetic hull due to the geomagnetic field [4];
- The wake magnetic field generated by the vehicle's motion disturbing the seawater flow and cutting through the geomagnetic field [5];
- The ocean wave magnetic field generated by the interaction of wind-driven surface waves with the geomagnetic field [6]. This kind of field is generally considered noise.

A magnetic anomaly field, present when the vehicle is both stationary and moving, is a static field that quickly diminishes with distance despite its large magnitude. In contrast,

a wake magnetic field, generated only during motion, persists for longer and over a larger domain [7].

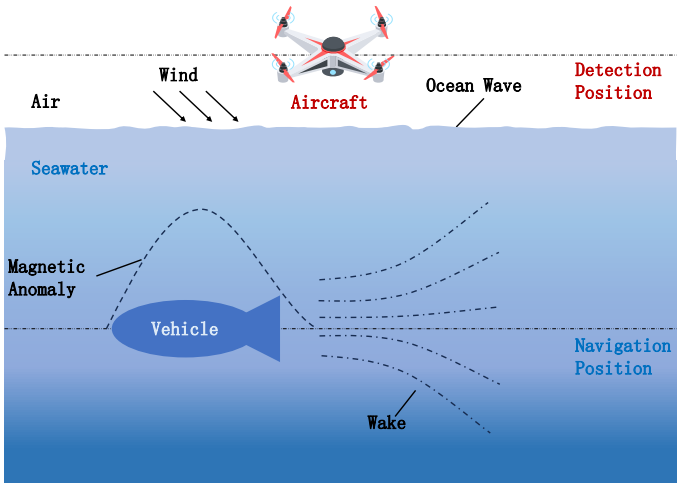

Figure 1. Schematic diagram of mechanism of magnetic anomaly generation.

Magnetic Anomaly Detection (MAD) is widely used to identify disturbances in the geomagnetic field generated by ferromagnetic underwater vehicles [8], and is based on mathematical models categorized as mathematical theory and magnetic body methods [9]. Among the former, the Finite Element Method (FEM) calculates magnetic fields by assessing the scalar magnetic potential in finite domains, and tools such as SIMULIA Opera [10], ANSYS Maxwell [11], and COMSOL Multiphysics [12] are widely used for modeling magnetic characteristics. In magnetic body methods, a hybrid model combining a rotating ellipsoid for the hull's magnetic signature [13] and a dipole array for the internal machinery enables efficient magnetic anomaly assessment [14]. Researchers have focused on the magnetic anomaly fields of stationary objects such as cables [15], pipelines [16], and sunken ships [17]. Under real-world conditions, vehicles usually move along certain courses at various depths [18], which directly leads to variations in the detection distance between vehicle and aircraft [19]; while this can be effectively modeled [20], the influence of a vehicle's speed on the spatial and temporal signatures of its magnetic field remains under-studied.

Underwater vehicles in seawater generate significant hydrodynamic wakes, including Kelvin [21], vortex [22], and internal wave wakes [23]. Kelvin wakes are the most significant, as they are surface waves [24], and their magnetic field can be modeled based on the wake wave height [25], and its spatial distribution is influenced by factors such as the vehicle's length [26], speed, and depth [27]. However, there is a gap in research regarding how changes in a vehicle's course affect the wake magnetic field, and the relevant temporal dynamics are not well understood. Additionally, the impact of navigational changes and conductivity on the wake magnetic field model has not been studied, nor has there been a combined study of the overall magnetic field resulting from the superposition of the magnetic anomaly and the wake magnetic fields.

In the context of underwater vehicle detection, it is crucial to consider the various sources of magnetic noise that can affect vehicle detectability, such as platform noise (up to 10 nT) [28], magnetic sensor noise (about 0.00087 nT) [29], and environmental noise (0.025–1 nT) [30]. Among these, environmental noise, especially ocean wave noise, is of particular interest in this study. Figure 1 indicates that ocean wave motion above the sea surface generates a magnetic field by interacting with the geomagnetic field. According to surface wave theory, the induced ocean wave magnetic field is correlated with wave height

and length, as described by the Weaver model [31]. Research on the variation in the induced magnetic field of multi-frequency ocean waves in finite-depth water [32], has shown that variations in seawater electrical conductivity can impact the magnetic fields generated by different wave types [33]. However, previous studies have primarily focused on deriving the expression of the induced magnetic field in the air layer, without investigating the effects of other factors, such as changes in wind speed and direction. Moreover, there is a lack of research on the temporal characteristics of ocean wave magnetic fields and the impact of ocean waves on a vehicle's magnetic field.

In summary, prior research has largely focused on separately analyzing the magnetic anomaly and wake magnetic fields of underwater vehicles, and the ocean wave magnetic field. Since magnetic sensors detect the composite magnetic field resulting from both the underwater vehicle and the environment, studying the spatiotemporal characteristics of these three fields together is crucial. This study aims to combine the modeling of these magnetic fields to clarify the spatiotemporal characteristics and attenuation patterns of the composite field, and analyze how it is affected by vehicle motion and marine environmental parameters.

The remainder of this paper is organized as follows: In Section 2, we cover the basic theories of the magnetic fields generated by underwater vehicles and ocean waves. In Section 3, we present simulations of magnetic fields in various scenarios, and in Section 4, we discuss their results. In Section 5, we present the conclusions of this study.

2. Basic Theory of Magnetic Fields of Underwater Vehicles

The magnetic fields generated by a vehicle and the ocean wave magnetic field are analyzed using the International Geomagnetic Reference Field (IGRF) model to describe the background geomagnetic field, and data from the World Ocean Atlas (WOA) to characterize the electrical conductivity of seawater. These varying magnetic fields are then combined to obtain a composite magnetic field.

2.1. Basic Model of the Geomagnetic Field

Considering the close relationship of the geomagnetic field, the vehicle-generated magnetic field, and the ocean wave magnetic field, it is essential to uniformly set the relevant parameters of the geomagnetic field. Within the computational domain, this field can be considered uniform, with constant magnitude and direction. To represent this, we adopted the latest IGRF-14 model [34]. As shown in Figure 2, the positive x-axis points to the geographic north, the positive y-axis points to the geographic west, and the positive z-axis is perpendicular to the xy-plane upwards.

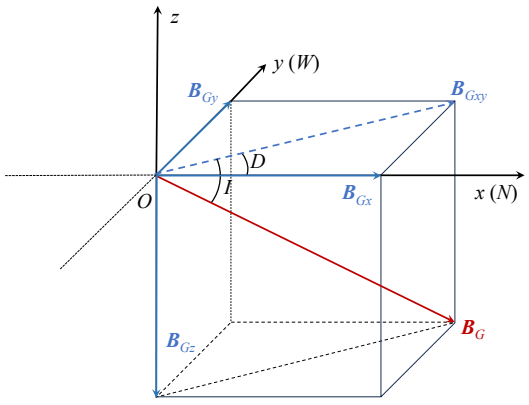

Figure 2. Schematic diagram of the geomagnetic field.

The projection of the geomagnetic induction intensity ($\boldsymbol{B}_G$) on the xy-plane is $\boldsymbol{B}_{Gxy}$, and the angle between them is the magnetic inclination, I, which is positive downward. The angle between $\boldsymbol{B}_{Gxy}$ and the northward direction is the magnetic declination, D, which is positive eastward. The geomagnetic induction intensity is expressed as

$$\boldsymbol{B}_G = gB \cdot (\boldsymbol{i} \cos I \cos D + \boldsymbol{j} \cos I \sin D - \boldsymbol{k} \sin I) \tag{1}$$

where gB represents the geomagnetic induction intensity; $\boldsymbol{i}$, $\boldsymbol{j}$, and $\boldsymbol{k}$ represent unit vectors along the x-, y-, and z-axes, respectively.

The values of the geomagnetic field vector intensity along the x-, y-, and z-axes of the coordinate system are denoted by $\boldsymbol{H}_{Gx}$, $\boldsymbol{H}_{Gy}$, and $\boldsymbol{H}_{Gz}$:

$$\begin{cases} \boldsymbol{H}_{Gx} = \boldsymbol{H}_G \cos I \cos D \\ \boldsymbol{H}_{Gy} = -\boldsymbol{H}_G \cos I \sin D \\ \boldsymbol{H}_{Gz} = \boldsymbol{H}_G \sin I \end{cases} \tag{2}$$

where $\boldsymbol{H}_G$ represents the geomagnetic field intensity, with $\boldsymbol{H}_G = \boldsymbol{B}_G / \mu_0$, where μ_0 is the permeability of free space, approximately $4\pi \times 10^{-7}$ H/m.

2.2. Mechanism of Magnetic Field Generation for Underwater Vehicles

The magnetic fields linked to the underwater vehicle itself are primarily of two types: the magnetic anomaly field due to ferromagnetic material and the wake magnetic field resulting from the vehicle's motion. Although these fields originate from distinct processes, they both intricately influence underwater vehicle detection, so it is necessary to understand their basic principles.

2.2.1. Magnetic Anomaly Field of a Ferromagnetic Underwater Vehicle

Magnetic anomalies are closely related to the inherent properties of ferromagnetic materials. The basic model for their calculation primarily consists of a combination of the FEM and magnetic body simulation. Here, the hybrid model is chosen for its accurate simulation of both the ferromagnetic shell and internal equipment's magnetic field, offering higher calculation accuracy and efficiency. The vehicle's hull is simplified as a rotating ellipsoidal model, where the ellipsoid's major axis corresponds to the length (l) of the underwater vehicle and the minor axis to its breadth (b). The magnetic dipoles are evenly distributed along the central axis of the ellipsoid, as shown in Figure 3. We take the center of the dipole model as the coordinate origin, the sea level as the xy-plane, and the direction perpendicular to the sea plane and upward as the z-axis, establishing a right-handed rectangular coordinate system. The geomagnetic field value in the geographic coordinate system is converted to the vehicle coordinate system; the course of the vehicle is θ_a, and the westward declination is positive.

The transformation relationship between the vehicle coordinate system and the geographic coordinate system for the vehicle magnetic field is obtained as

$$\begin{cases} \boldsymbol{H}_{Gx'} = \boldsymbol{H}_{Gx} \cos \theta_a + \boldsymbol{H}_{Gy} \sin \theta_a \\ \boldsymbol{H}_{Gy'} = -\boldsymbol{H}_{Gx} \sin \theta_a + \boldsymbol{H}_{Gy} \cos \theta_a \\ \boldsymbol{H}_{Gz'} = \boldsymbol{H}_{Gz} \end{cases} \tag{3}$$

where the subscripts x', y', and z' represent the vehicle coordinate system, while x, y, and z represent the geographic coordinate system.

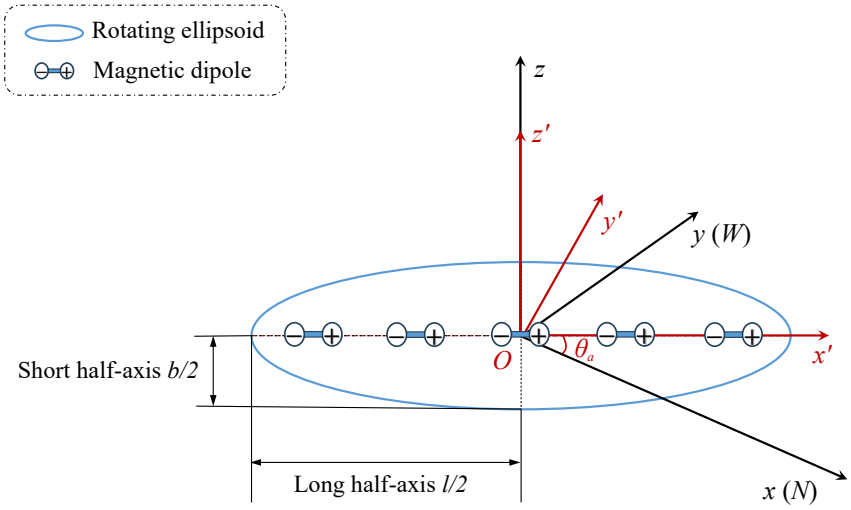

Figure 3. Schematic diagram of hybrid model of underwater vehicle's magnetic anomaly field.

Firstly, the radiated magnetic field of the electromechanical equipment inside the underwater vehicle is obtained based on the magnetic dipole array model. According to the magnetization law of an ellipsoid model in an external field, the three components of the vehicle's magnetic moment have a functional relationship with the three components of the geomagnetic field, which can be expressed with specific formulas:

$$\begin{cases} \boldsymbol{M}_x = \dfrac{\pi l b^2}{6(1+L)} \cdot \boldsymbol{H}_{Gx'} \\ \boldsymbol{M}_y = \dfrac{\pi l b^2}{6(1+S)} \cdot \boldsymbol{H}_{Gy'} \\ \boldsymbol{M}_z = \dfrac{\pi l b^2}{6(1+S)} \cdot \boldsymbol{H}_{Gz'} \end{cases} \tag{4}$$

where $\boldsymbol{M}_x$, $\boldsymbol{M}_y$, and $\boldsymbol{M}_z$ are the magnetic moments of the magnetic dipole along the x-, y-, and z-axes, respectively; L and S are the demagnetization factors in the long- and short-axis directions of the vehicle, respectively. The empirical formulas for the demagnetization factors of ellipsoidal ferromagnet are as follows [35]:

$$\begin{cases} L = \dfrac{1}{\lambda^2-1}\left[\dfrac{\lambda}{\sqrt{\lambda^2-1}}\ln(\lambda+\sqrt{\lambda^2-1})-1\right] \\ S = \dfrac{\lambda^2}{2(\lambda^2-1)}\left[1-\dfrac{1}{\lambda\sqrt{\lambda^2-1}}\ln(\lambda+\sqrt{\lambda^2-1})\right] \end{cases} \tag{5}$$

where λ is the ratio of the long and short semi-axes of the ellipsoid model and $\lambda = l/b$.

The magnetic anomaly vector fields ($\boldsymbol{H}_{dx}$, $\boldsymbol{H}_{dy}$, and $\boldsymbol{H}_{dz}$) of the magnetic dipole array at detection point P are expressed as [36]

$$\begin{bmatrix} \boldsymbol{H}_{dx} \\ \boldsymbol{H}_{dy} \\ \boldsymbol{H}_{dz} \end{bmatrix} = \sum_{n=1}^{N} \frac{1}{4\pi \|\boldsymbol{r}_{pn}\|_2^5} \begin{bmatrix} a_x & a_y & a_z \\ b_x & b_y & b_z \\ c_x & c_y & c_z \end{bmatrix} \begin{bmatrix} \boldsymbol{M}_x \\ \boldsymbol{M}_y \\ \boldsymbol{M}_z \end{bmatrix} \tag{6}$$

where N is the total number of magnetic dipoles. The coefficients of the coefficient matrix are as follows [37]:

$$\begin{cases} a_x = 3(x_p - u_n)^2 - \|\boldsymbol{r}_{pn}\|_2^2 \\ b_y = 3(y_p - v_n)^2 - \|\boldsymbol{r}_{pn}\|_2^2 \\ c_z = 3(z_p - w_n)^2 - \|\boldsymbol{r}_{pn}\|_2^2 \\ a_y = b_x = 3(x_p - u_n)(y_p - v_n) \\ a_z = c_x = 3(x_p - u_n)(z_p - w_n) \\ b_z = c_y = 3(y_p - v_n)(z_p - w_n) \end{cases} \tag{7}$$

where $\boldsymbol{r}_{pn} = \boldsymbol{r}_p - \boldsymbol{r}_n$ is the distance from the p_{th} detection point ($\boldsymbol{r}_p = \begin{bmatrix} x_p & y_p & z_p \end{bmatrix}^{\mathrm{T}}$) to the n_{th} dipole ($\boldsymbol{r}_n = \begin{bmatrix} u_n & v_n & w_n \end{bmatrix}^{\mathrm{T}}$). The x-coordinate of the magnetic dipole is $u_n = [n - (N+1)/2]\Delta r \cos\theta_a$, and the dipole spacing is $\Delta r = l/(N-1)$. The relationship between the total magnetic anomaly field ($\boldsymbol{H}_d$) and the vector fields is

$$|\boldsymbol{H}_d| = \sqrt{|\boldsymbol{H}_{dx}|^2 + \left|\boldsymbol{H}_{dy}\right|^2 + |\boldsymbol{H}_{dz}|^2} \tag{8}$$

Therefore, the intensity of the magnetic anomaly field can be obtained, and the magnetic anomaly induction intensity can be derived as

$$\boldsymbol{B}_d = \mu_0 \boldsymbol{H}_d \tag{9}$$

Then, the rotating ellipsoid model is established to simulate the hull of the vehicle, and the FEM is employed to solve for its radiated magnetic field. We solve for the magnetic anomaly field of an ellipsoid by choosing the Steady method, according to Gauss's magnetic law:

$$\nabla \cdot \boldsymbol{H}_e = 0 \tag{10}$$

where $\boldsymbol{H}_e$ represents the ellipsoid's magnetic anomaly field intensity, given by

$$\boldsymbol{H}_e = -\nabla V_m + \boldsymbol{H}_G \tag{11}$$

where V_m represents the reference magnetic potential. We substitute Equation (11) into Equation (10) to obtain the differential equation

$$-\nabla \cdot (\nabla V_m + \boldsymbol{H}_G) = 0 \tag{12}$$

The insulating boundary condition of the geomagnetic field at the external boundary of the computational domain is set as follows:

$$\boldsymbol{n} \cdot (\boldsymbol{H}_G + \boldsymbol{H}_e) = \boldsymbol{n} \cdot \boldsymbol{H}_G \tag{13}$$

where $\boldsymbol{n}$ is the boundary normal vector of the ellipsoid's outer surface. Equation (13) can be further simplified to

$$-\boldsymbol{n} \cdot \boldsymbol{H}_e = 0 \tag{14}$$

Therefore, the magnetic anomaly field intensity can be determined, and the magnetic anomaly induction intensity of an ellipsoid can be derived as

$$\boldsymbol{B}_e = \mu_0 \mu_r \boldsymbol{H}_e \tag{15}$$

where μ_r is the relative magnetic permeability of the hull material and $\mu_r \gg 1$.

Finally, the total magnetic anomaly induction intensity of the equivalent hybrid model can be obtained through superimposition:

$$\boldsymbol{B}_a = \boldsymbol{B}_d + \boldsymbol{B}_e \tag{16}$$

The basic parameters of a specific underwater vehicle at a given location can be identified, and this information enables the quantitative calculation of the magnetic anomaly intensity induced by the hybrid model by using Equation (16).

2.2.2. Wake Magnetic Field of an Underwater Vehicle in Motion

When an underwater vehicle travels at a constant speed along a path aligned with the positive x-axis in seawater, it generates free surface waves. These waves include both diffusion and transverse waves, creating a Kelvin wake as depicted in Figure 4. The most significant surface fluctuations occur within a range of 16° to 19.5° (half divergence angle) on either side of the vehicle's trajectory, forming a V-shaped pattern overall [38].

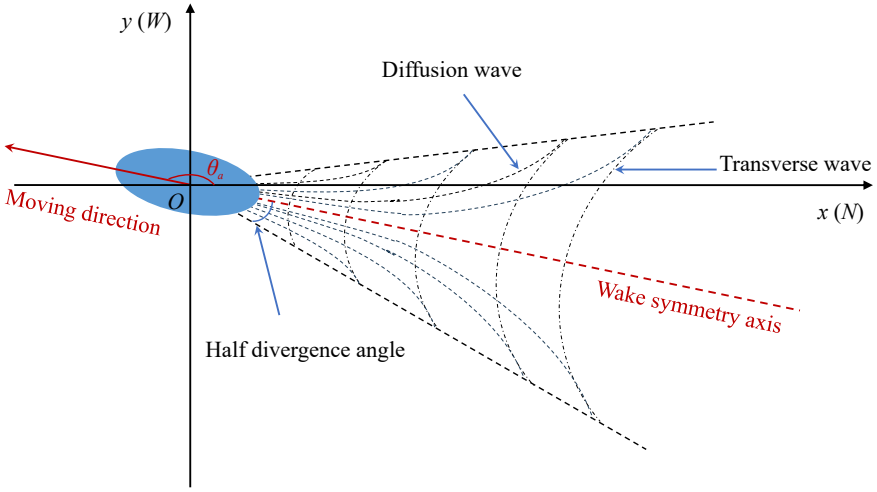

Figure 4. Schematic diagram of Kelvin wake generated by moving vehicle.

Using the above-mentioned rotating ellipsoid model to describe underwater vehicles, the free-wake spectrum function can be expressed as follows [39]:

$$S_w(\theta_w) = \left(\frac{2s_w\Delta}{\pi l}\right)\sin\left(\frac{q_w l\cos\theta_w}{2}\right) \tag{17}$$

where Δ is the vehicle's volume, with $\Delta = \pi l b^2/6$; q_w is the wake's wavenumber, with $q_w = g/[s_w^2\cos^2(\theta_w - \theta_a)]$; s_w is the vehicle's speed; g is the gravitational acceleration, approximately 9.81 m/s^2; and θ_w is the wake's propagation direction, which varies within $\pi/2$ on both sides of the symmetry axis, which is indicated by the red dashed line in Figure 4.

Assuming that seawater is an incompressible fluid with constant volume, it meets the continuity equation $\nabla \cdot V_w = 0$. The wake velocity field can be expressed as [39]

$$\boldsymbol{V}_w(x,y,z,t) = \mathrm{Re}\int_{-\pi/2}^{\pi/2} S_w(\theta_w)\boldsymbol{v}_w \exp[-i(\omega_w t + q_w x\cos\theta_w + q_w y\sin\theta_w)]d\theta \tag{18}$$

where t is time and ω_w is the wake's angular frequency, with $\omega_w = q_w s_w\cos\theta_w$. The vector $\boldsymbol{v}_w$ is given by

$$\boldsymbol{v}_w = q_w^2\exp[q_w(d_a + d_v)](i\cos\theta_w, i\sin\theta_w, -1) \tag{19}$$

where d_a is the detection height of the aircraft and d_v is the diving depth of the vehicle.

According to Faraday's law of electromagnetic induction, as the wake velocity vector ($\boldsymbol{V}_w$) crosses the geomagnetic field vector ($\boldsymbol{H}_G$), the electric field ($\boldsymbol{E}_w$) is induced perpendicularly to both, which in turn generates current density. Therefore, the relationship between the wake magnetic field ($\boldsymbol{H}_w$) and the velocity field ($\boldsymbol{V}_w$) satisfies the following Maxwell equations:

$$\begin{cases} \nabla \times \boldsymbol{H}_w = \sigma_i \boldsymbol{E}_w + \sigma_i \mu_0 (\boldsymbol{V}_w \times \boldsymbol{H}_G) + \varepsilon_i \dfrac{\partial \boldsymbol{E}_w}{\partial t} \\ \nabla \cdot \boldsymbol{H}_w = 0 \\ \nabla \times \boldsymbol{E}_w = -\mu_0 \dfrac{\partial \boldsymbol{H}_w}{\partial t} \end{cases} \tag{20}$$

where σ_i and ε_i are the electrical conductivity and dielectric constant of the medium, respectively; and the subscripts $i = 0, 1$ correspond to the air and seawater domains, respectively.

In this study, WOA23 temperature and salinity data from the WOA [40] are used for the precise calculation of seawater electrical conductivity, which is given by

$$C(S, T, P) = R \cdot C(35, 15, 0) \cdot r_T \cdot r_P \tag{21}$$

where S is the salinity; T is the temperature; P is the seawater pressure, which is dependent on sea depth; R is the conductivity ratio; $C(35, 15, 0)$ is the standard seawater electrical conductivity, with a value of 4.2914 S/m; r_T and r_P are temperature and pressure correction factors, respectively.

Assuming that the influence of the seabed is disregarded and considering that the wave height of free surface waves in seawater is much smaller than their length, the free surface is approximated to a plane $z = 0$ based on the following identical equation [41]:

$$\nabla \times (\nabla \times \boldsymbol{H}_w) = \nabla(\nabla \cdot \boldsymbol{H}_w) - \nabla^2 \boldsymbol{H}_w \tag{22}$$

We take the curl on both sides of the first expression in Equation (20), substitute the third expression, and simplify Equation (22) to obtain the following differential equation:

$$-\nabla^2 \boldsymbol{H}_w = -\sigma_i \mu_0 \left[\frac{\partial \boldsymbol{H}_w}{\partial t} - \nabla \times (\boldsymbol{V}_w \times \boldsymbol{H}_G) \right] - \varepsilon_i \mu_0 \frac{\partial^2 \boldsymbol{H}_w}{\partial t^2} \tag{23}$$

Equation (23) represents a linear expression. In our research study, we only need to consider a single harmonic component by accounting for the angular frequency (ω_w). The wake magnetic field intensity generated by an underwater vehicle which satisfies the above differential equation can be expressed as [41]

$$\boldsymbol{H}_w(x, y, z, t) = \mathrm{Re} \int_{-\pi/2}^{\pi/2} S_w(\theta_w) \boldsymbol{h}_w \exp[-i(\omega_w t + q_w x \cos\theta_w + q_w y \sin\theta_w)] d\theta \tag{24}$$

where the vector $\boldsymbol{h}_w$ is given by

$$\boldsymbol{h}_w = \left[\boldsymbol{\alpha}_w - \frac{\boldsymbol{\beta}_w}{q_w^2 - \delta_w^2} \right] \exp(-\gamma_w d_a) \tag{25}$$

where $\boldsymbol{\alpha}_w$ and $\boldsymbol{\beta}_w$ are the wake's amplitude and phase vectors, respectively. These are given by

$$\boldsymbol{\alpha}_w = \frac{(q_w + \gamma_w)}{(\delta_w + \gamma_w)} \frac{\boldsymbol{\beta}_w \cdot \boldsymbol{k}}{(q_w^2 - \delta_w^2)} \cdot \left(\frac{\delta_w \cos\theta_w}{i q_w}, \frac{\delta_w \sin\theta_w}{i q_w}, 1 \right) \tag{26}$$

$$\boldsymbol{\beta}_w = \mu_0 \sigma_1 q_w^3 \exp(-q_w d_a) [(\boldsymbol{H}_G \cdot \boldsymbol{k}) - i(\boldsymbol{H}_G \cdot \boldsymbol{r}_w)] \cdot (i \cos\theta_w, i \sin\theta_w, -1) \tag{27}$$

respectively, where δ_w and γ_w are the propagation parameters of the vehicle wake in the medium, with $\delta_w^2 = q_w^2 - \varepsilon_1\mu_0\omega_w^2 - i\sigma_1\mu_0\omega_w$ and $\gamma_w^2 = q_w^2 - \varepsilon_0\mu_0\omega_w^2$.

Substituting Equations (26) and (27) into Equation (25) gives $\boldsymbol{h}_w$; then, $\boldsymbol{H}_w$ can be obtained from Equation (24). Therefore, the wake magnetic field can be obtained, and the wake magnetic induction intensity can be derived as

$$\boldsymbol{B}_w = \mu_0 \boldsymbol{H}_w \tag{28}$$

2.3. Mechanism of Magnetic Field Generation for Ocean Waves

Waves are relatively common movements of seawater caused by wind, and they usually occur on the sea surface, as shown in Figure 5. The red arrows show the wind direction, with the arrow length indicating the speed of the wind field. Moreover, the direction of the black streamline fluctuations indicates the direction of ocean wave undulations, where denser streamlines indicate higher velocity. The blue coloration in Figure 5 represents the volume fraction of seawater: lighter shades denote areas with a lower volume fraction of seawater, while darker shades indicate regions with a higher volume fraction.

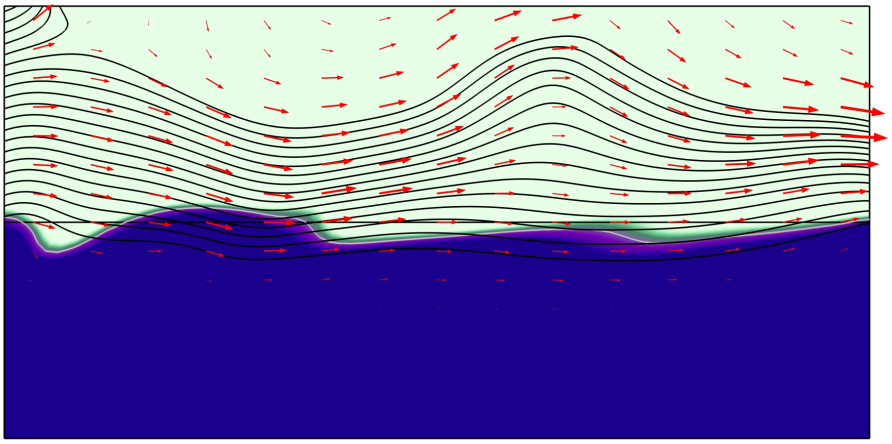

Figure 5. Schematic diagram of wind generating ocean waves.

The wave spectrum is a Fourier transform that describes the correlation function of sea surface undulations, and represents the frequency distribution of wave energy relative to its constituent waves [42]. Since the Joint North Sea Wave Project (JONSWAP) spectrum is regarded as the international standard wave spectrum, the wave spectrum in this study ($S_m(\theta_n)$) is represented by the JONSWAP spectrum [43] and the direction spectrum proposed by Cote [44]:

$$S_m(\theta_n) = \frac{3.3^K J g^2}{\pi\omega_m^2} \exp\left(-\frac{1.25\omega_p^4}{\omega_m^4}\right) \cdot \left[1 + A\cos 2(\theta_n - \theta_p) + F\cos 4(\theta_n - \theta_p)\right] \tag{29}$$

where θ_p is the wind direction angle between the wind's propagation direction and the x-axis; θ_n is the wave's propagation direction, ranging within $\pi/2$ on both sides of θ_p. The parameters A and F in the Cote direction spectrum are given by

$$A = 0.5 + 0.82\exp\left(-\frac{\omega_m^2}{2\omega_p^2}\right) \tag{30}$$

$$F = 0.32\exp\left(-\frac{\omega_m^2}{2\omega_p^2}\right) \tag{31}$$

and the parameters K and J in the JONSWAP spectrum are given by

$$K = \exp\left[-\frac{(\omega_m - \omega_p)^2}{0.0162\omega_p^2}\right] \tag{32}$$

$$J = 0.076\left(\frac{g \cdot 10^6}{s_p^2}\right)^{-0.22} \tag{33}$$

where ω_m is the ocean wave angular frequency, which satisfies the dispersion relationship $\omega_m^2 = gq_m$; q_m is the ocean wavenumber; ω_p is the wind angular frequency, with $\omega_p = 22 \cdot 10^{-1.98} g^{0.67}/s_p^{1.66}$; and s_p is the wind speed 19.5 m above sea level.

Recent studies have shown that wave dynamics such as tidal effects and Large-Scale Coherent Structures can influence the movement of targets in the ocean to a certain extent, specifically influencing formation and propagation, especially in long-period waves [45]. To facilitate the subsequent linear superposition of various magnetic fields and efficiently investigate the impact of individual parameters on the resulting composite magnetic field, this study employs a simplified mathematical model of ocean waves to derive solutions. Ocean waves can be described as the linear superposition of $M \times M$ sine waves, and their velocity field can be expressed as [46]

$$\boldsymbol{V}_m(x, y, z, t) = \mathrm{Re}\sum_{m=1}^{M}\sum_{n=1}^{M} \boldsymbol{v}_m \exp[-i(\omega_m t + q_m x\cos\theta_n + q_m y\sin\theta_n + \varphi_{mn})] \tag{34}$$

where M is the number of both frequency and propagation; φ_{mn} is the initial phase, which is randomly distributed within $(0, 2\pi)$; and the vector $\boldsymbol{v}_m$ is given by

$$\boldsymbol{v}_m = a_m\omega_m \exp(q_m d_a)(i\cos\theta_n, i\sin\theta_n, -1) \tag{35}$$

where a_m is the amplitude and $a_m = \sqrt{2S_m(\theta_n)\Delta\omega\Delta\theta}$.

Similar to that of wakes, the magnetic field of ocean waves is also induced by the latter's velocity field driven by the wind. By replacing the subscript w with m and the integration operation with the summation operation in Equations (20) and (23), we express the ocean waves' magnetic field as [46]

$$\boldsymbol{H}_m(x, y, z, t) = \mathrm{Re}\sum_{m=1}^{M}\sum_{n=1}^{M} \boldsymbol{h}_m \exp[-i(\omega_m t + q_m x\cos\theta_n + q_m y\sin\theta_n + \varphi_{mn})] \tag{36}$$

where the vector $\boldsymbol{h}_m$ is given by

$$\boldsymbol{h}_m = \left[\boldsymbol{\alpha}_m - \frac{\boldsymbol{\beta}_m}{q_m^2 - \delta_m^2}\right]\exp(-\gamma_m d_a) \tag{37}$$

where $\boldsymbol{\alpha}_m$ and $\boldsymbol{\beta}_m$ are the ocean waves' amplitude and phase vectors. These are given by

$$\boldsymbol{\alpha}_m = \frac{(q_m + \gamma_m)}{(\delta_m + \gamma_m)}\frac{\boldsymbol{\beta}_m \cdot \boldsymbol{k}}{(q_m^2 - \delta_m^2)} \cdot \left(\frac{\delta_m\cos\theta_n}{iq_m}, \frac{\delta_m\sin\theta_n}{iq_m}, 1\right) \tag{38}$$

$$\boldsymbol{\beta}_m = \mu_0\sigma_1 q_m^3 \exp(-q_m d_a)[(\boldsymbol{H}_G \cdot \boldsymbol{k}) - i(\boldsymbol{H}_G \cdot \boldsymbol{r}_m)] \cdot (i\cos\theta_n, i\sin\theta_n, -1) \tag{39}$$

respectively, where δ_m and γ_m are the propagation parameters of ocean waves in the medium, with $\delta_m^2 = q_m^2 - \varepsilon_1\mu_0\omega_m^2 - i\sigma_1\mu_0\omega_m$ and $\gamma_m^2 = q_m^2 - \varepsilon_0\mu_0\omega_m^2$.

Substituting Equations (38) and (39) into Equation (37) gives $\boldsymbol{h}_m$; then, $\boldsymbol{H}_m$ can be obtained from Equation (36). Therefore, the ocean wave magnetic field can be obtained, and the ocean wave magnetic induction intensity can be derived as

$$\boldsymbol{B}_m = \mu_0 \boldsymbol{H}_m \tag{40}$$

By comparing the derivation processes of the expressions of vehicle wake and ocean wave magnetic fields in this study, it is found that they present great similarity, and the structure of the obtained coefficient expressions is the same. Because vehicle wake and ocean waves are both long gravity waves that occur on the sea surface, their similar kinematic behavior leads to analogous mathematical formulations and functional structures in their simulation theories. Additionally, the models assume a consistent geomagnetic field, which results in similar expressions for the magnetic fields generated by the motion of seawater.

2.4. Composite Magnetic Field Solution Method for Navigation Vehicles in the Presence of Ocean Waves

To obtain the composite magnetic induction intensity, we apply the principle of linear superposition, which is valid under the assumptions of the linearity and additivity of the individual magnetic fields. The magnetic anomaly induction intensity ($\boldsymbol{B}_a$), wake magnetic induction intensity ($\boldsymbol{B}_w$) and ocean wave magnetic induction intensity ($\boldsymbol{B}_m$) are superimposed to obtain the composite magnetic induction intensity ($\boldsymbol{B}_c$) as

$$\boldsymbol{B}_c = \boldsymbol{B}_a + \boldsymbol{B}_w + \boldsymbol{B}_m \tag{41}$$

which simplifies the analysis by considering each component separately before integrating it with the others to form a comprehensive view of the composite magnetic field.

The solution process for the composite magnetic field is illustrated in Figure 6. By integrating these magnetic fields, a more comprehensive analysis of the detected magnetic field can be conducted. The composite magnetic field includes the magnetic anomaly and wake magnetic fields generated by the underwater vehicle, which are the signals of interest, and the magnetic field generated by ocean waves, which acts as noise in this context.

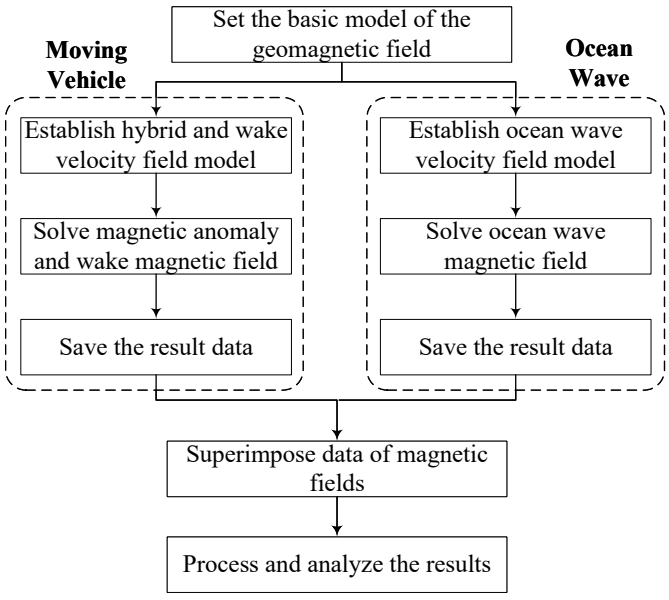

Figure 6. Solution flowchart of composite magnetic field.

Under the quasi-static limit, the changes in the magnetic field are slow compared with the vehicle's motion and the wave dynamics. This enables us to treat the magnetic field as essentially static over the short timescale of these dynamic processes, simplifying analyses and calculations. This approximation is valid when

$$\frac{\tau_B}{\tau_D} \gg 1 \tag{42}$$

where τ_B is the timescale of the changes in the magnetic field and τ_D is the timescale of the dynamic processes.

In our scenario, adjustments to the magnetic field happen over a period of minutes, whereas changes in the vehicle's speed and the dynamics of the waves occur within seconds. Consequently, the magnetic field can be approximated as quasi-static, meaning that it changes slowly enough relative to the fast dynamics of vehicle motion and wave interactions, which validates the use of this approximation in our analysis.

3. Simulation Results of Underwater Vehicle's Magnetic Fields

The simulations presented in the following provide a detailed examination of an underwater vehicle's magnetic field characteristics under multiple conditions. We first address the complexities involved in modeling and analyzing the magnetic fields generated by underwater vehicles, laying the foundation for the subsequent discussion on the magnetic fields of a vehicle below a calm sea surface and the composite magnetic field of a vehicle in the presence of ocean waves.

3.1. Problem Description

According to the IGRF-14 model, we set the observation position as the sea area at 16°15′50″ N and 109°40′12″ E, and calculate the geomagnetic induction intensity, the magnetic inclination and declination angles, as shown in Table 1. The geomagnetic induction intensity is primarily directed along the x-axis, with the z-axis component being the next-most significant and the y-axis component being the smallest.

Table 1. Calculation results of geomagnetic field parameters.

Parameter	Value	Unit
Geomagnetic induction intensity	43,187.70	nT
Magnetic inclination angle	22.01	deg
Magnetic declination angle	−1.62	deg
x-Component of intensity	40,024.96	nT
y-Component of intensity	−1132.79	nT
z-Component of intensity	16,183.22	nT

Figure 7 shows the relative positional relationship between the aircraft detection points and the moving underwater vehicle, where the blue ellipse represents the starting position of the vehicle; the diving depth is set to 80 m, and the vehicle moves at a constant speed along the QQ' route in the negative x-axis direction. The red circle represents the detection point of the aircraft, which is located at point P, and the detection height is set to 50 m.

Detection distance $|PQ|$ represents the Closest-Path Approach (CPA) length between the detection point and the moving vehicle [47] and can be expressed as

$$|PQ| = \sqrt{\left(|P'O'| + |PO'|\right)^2 + \left(|P'Q|\right)^2} \tag{43}$$

where $|P'O'|$ is the vertical distance between the moving vehicle and the sea level, $|PO'|$ is the vertical distance between the detection point and the sea level, and $|P'Q|$ is the horizontal distance between the point and the vehicle. The time duration (t) is

$$t = |P'Q|/s_w \tag{44}$$

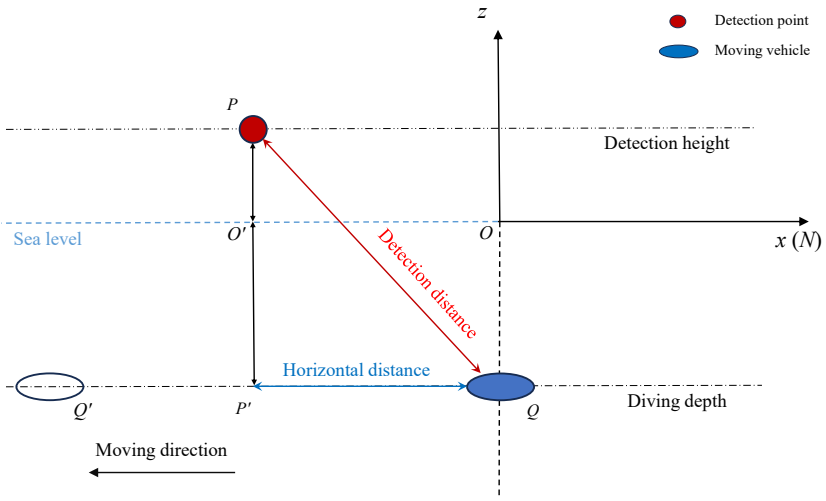

Figure 7. A 2D vertical view of the relative position between detection point and the moving vehicle.

The entire computational domain is divided into seawater ($z < 0$) and air ($z > 0$). The electrical conductivity of seawater is taken at a depth of 10 m, calculated to be 5.07 S/m (refer to Equation (21)), and the relative permittivity of seawater is set to 80. The joint model of the underwater vehicle and the computing domain is shown in Figure 8. The vehicle is located inside the sea area, the detection plane is within the air domain and parallel to the sea level, and the detection path is a straight line along the x-axis ($y = 0$).

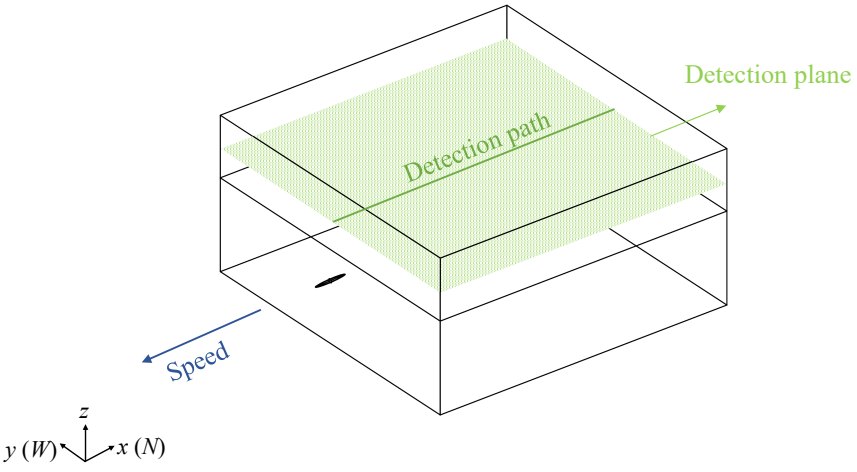

Figure 8. Schematic diagram of the detection plane and path within the computational domain.

The computational domain's outer boundary is set far from the vehicle to ensure that the boundary conditions have no effect on the simulation results. It extends over ten times the maximum wavelength in all directions from the vehicle. We apply boundary conditions to simulate the air–seawater environment by using a 2D projection of the 3D domain equation for the vehicle's hull, which includes the hull's thickness and permeability. This method effectively models highly permeable thin sheets and aligns the boundary conditions with the background magnetic field.

The main parameters of the simulation model are shown in Table 2. To enhance stability, the aspect ratio of the vehicle is set to 8.8. The hull of the underwater vehicle is made of high-strength steel that can withstand extremely-high water pressure [48]. After demagnetization, the relative magnetic permeability of the hull usually drops significantly, ranging from 100 to 300 [49]. Finally, the vehicle model is divided with the custom meshing method, yielding 179,026 boundary elements and 2174 edge elements.

Table 2. Main parameter settings for vehicle model simulation.

Parameter	Value	Unit
Molded length	107.6	m
Molded breadth	12.2	m
Hull thickness	0.05	m
Relative permeability	200	-
Maximum element size	10	m
Minimum element size	2	m
Maximum element growth rate	1.5	-
Curvature factor	0.2	-
Resolution of narrow regions	0.5	-

A mesh convergence study was conducted to validate the independence of our results from the mesh size and boundary conditions. It involved refining the mesh incrementally and monitoring the change in the magnetic field intensity at key points within the domain; the mesh was considered converged when the relative change in magnetic field intensity fell below 1% between successive refinements. The convergence graph in Figure 9 illustrates the mesh refinement and the corresponding changes in magnetic field intensity, showing that the error gradually decreases with the increase in the number of iterations and eventually stabilizes or reaches the preset convergence standard. This indicates that the calculation process is convergent and that the result is relatively accurate.

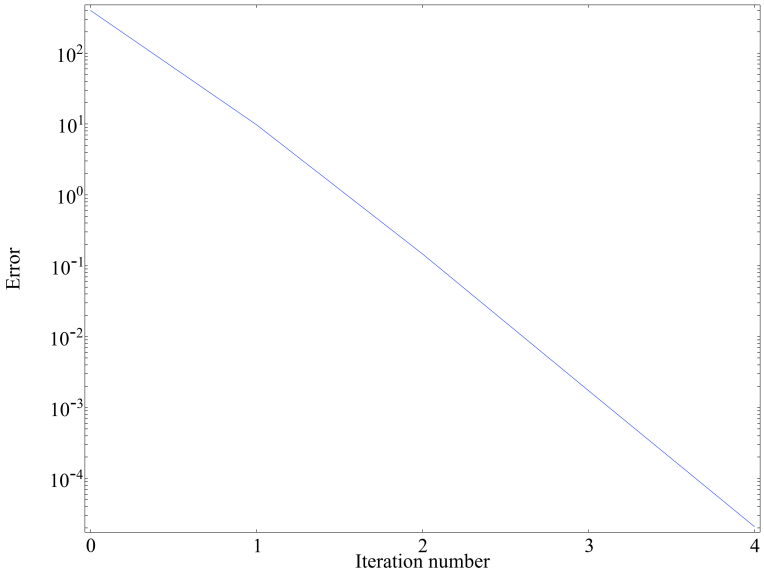

Figure 9. Mesh convergence graph check of vehicle model.

3.2. Different Magnetic Fields of a Vehicle Under a Calm Sea Surface

In this section, we present the analysis of the vehicle's magnetic fields under calm sea conditions, starting with the scenario where there are no ocean waves. When stationary, the vehicle induces only a magnetic anomaly field, while when motion, it induces

both a magnetic anomaly field and a wake magnetic field, which form the total vehicle magnetic field.

3.2.1. Magnetic Field Distribution of Vehicle at Starting Position

Initially, we examine the scenario of the vehicle's starting position at a depth of 80 m, denoted by point Q in Figure 7. When stationary along the negative x-axis, the underwater vehicle generates only a magnetic anomaly field. The magnetic anomaly fields obtained on the detection plane by using the rotating ellipsoid model and the hybrid model are shown in Figure 10. Specifically, Figure 10b shows that the magnetic anomaly distribution of the ellipsoid model is concentrated, with a peak magnetic induction intensity of approximately 59.52 nT. In contrast, the hybrid model in Figure 10d, which combines an ellipsoid model and an array of five magnetic dipoles, generates a stronger magnetic anomaly field, with a peak magnetic induction intensity of approximately 62.51 nT. It can be clearly seen that the contour pattern of the hybrid model is more elongated, reflecting the influence of the magnetic dipole array source in the hybrid model.

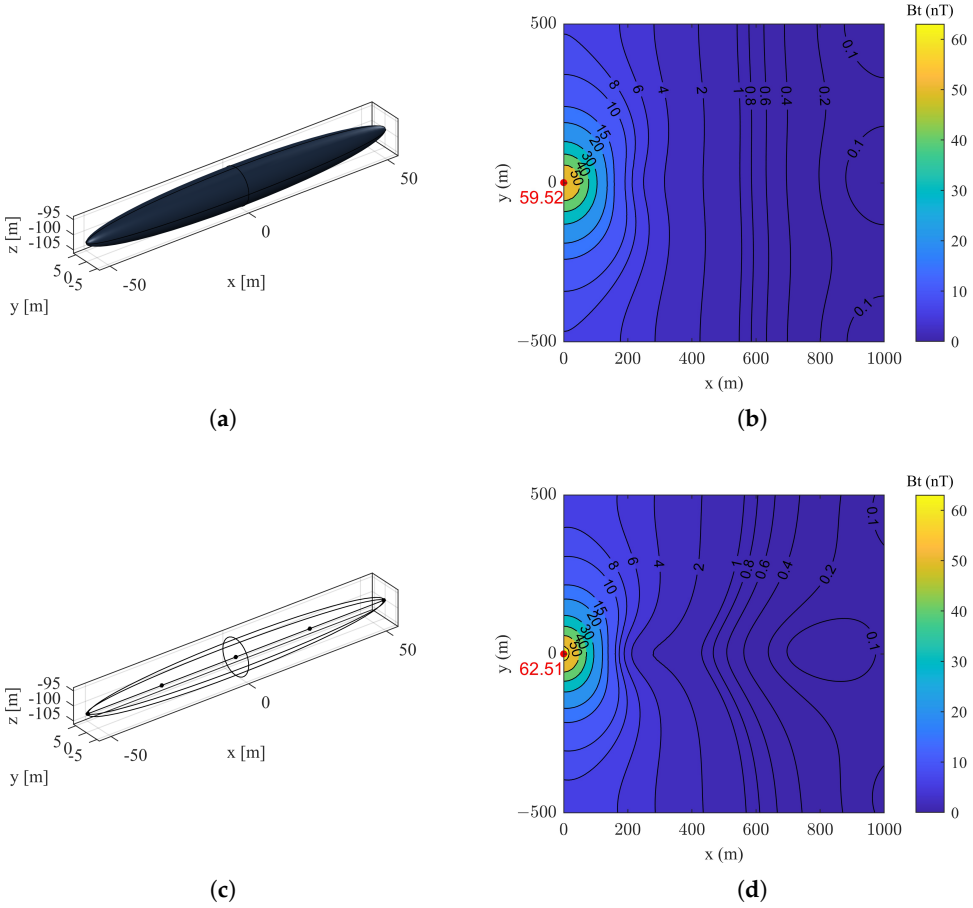

Figure 10. Magnetic anomaly fields of different models on detection plane. (**a**) Ellipsoid model. (**b**) Magnetic anomaly field of ellipsoid model. (**c**) Hybrid model. (**d**) Magnetic anomaly field of hybrid model.

When the underwater vehicle maintains starting position depth Q and sails at a speed of 20 kn, it induces an integrated magnetic field along the detection path shown in Figure 11, which includes both a magnetic anomaly field and a wake magnetic field. Figure 11a displays the magnetic anomaly vector fields, where the x-, y-, and z-components periodically vary along the x-axis. Moreover, Figure 11b displays the integrated magnetic field, which decays more slowly, extending the detection range and improving underwater vehicle tracking. The standard deviation analysis indicates that the x- and z-components of

the magnetic fields exhibit significant differences, with standard deviations of 1.6155 nT and 1.6284 nT, respectively. In contrast, the y-component shows negligible standard deviation, 0.0013 nT, implying minimal influence on the overall magnetic field distribution along the detection path.

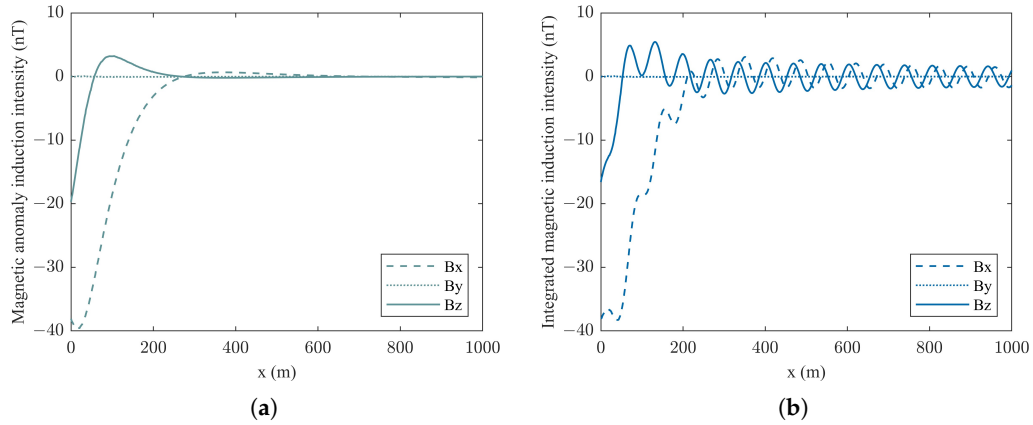

(**a**) (**b**)

Figure 11. Magnetic fields of moving vehicle along detection path. (**a**) Magnetic anomaly field attenuation. (**b**) Integrated magnetic field attenuation.

Since the wake magnetic field is superimposed on the magnetic anomaly field during the vehicle's movement, the influence of different course angles on the detection plane at the initial moment on the integrated magnetic field is investigated, as shown in Figure 12. As the vehicle's course changes, so does the integrated magnetic field's pattern and intensity, showing that the direction greatly influences the detected magnetic signature. The wake magnetic field overlays the magnetic anomaly field, spreads, and changes in intensity with different courses, suggesting that the course affects magnetic detection. Importantly, the wake magnetic field distribution is symmetric with respect to the vehicle's course.

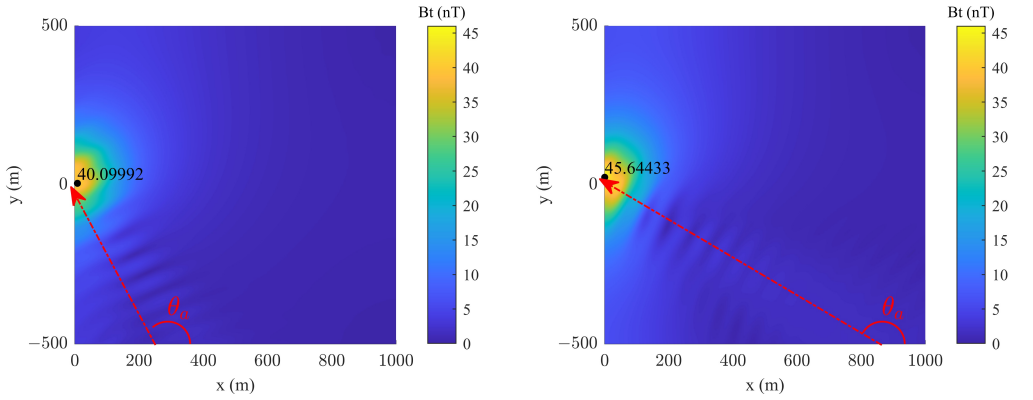

(**a**) (**b**)

Figure 12. Influence of course on vehicle magnetic field at initial moment. (**a**) Course angle of 120°. (**b**) Course angle of 150°.

3.2.2. Variation in Magnetic Field of Vehicle in Motion

If we suppose that the vehicle is moving at a constant speed in a straight line from point $Q(0, 0, -80)$, it can be inferred from Equation (17) that, in theory, its speed influences the wake magnetic spectrum, thereby affecting the wake magnetic field. The simulation results of the temporal characteristics of the magnetic anomaly field and the vehicle's integrated magnetic field at different speeds at detection point $P(-500, 0, 50)$ are illustrated in Figure 13. The magnetic anomaly field intensity remains consistent over time regardless of the vehicle's speed, confirming that speed does not influence intensity. On the other hand,

the vehicle's integrated magnetic field, which includes both the magnetic anomaly field and the wake magnetic field, exhibits a distinct difference in peak intensity and duration at the two speed values. A higher speed results in higher peak intensity but shorter duration, indicating that while speed does not affect the magnetic anomaly field, it significantly impacts the wake magnetic field characteristics.

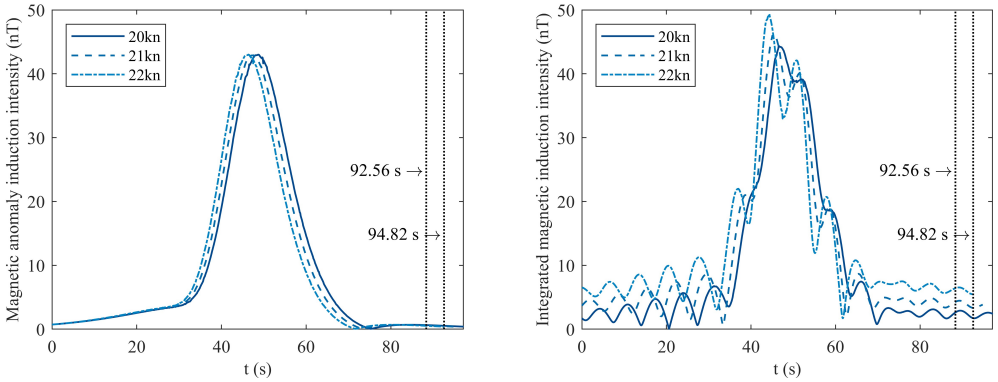

(**a**) (**b**)

Figure 13. Temporal distribution of total magnetic field at different speed. (**a**) Magnetic anomaly field. (**b**) Vehicle's integrated magnetic field.

When the vehicle moves to midpoint $P'(-500, 0, -80)$ (refer to Figure 7), it is positioned directly below detection point P; thus, the magnetic induction intensity is at its peak at approximately 48 s, as shown in Figure 13. The influence of the diving depth on the vehicle's magnetic fields at detection point P is shown in Figure 14. The intensity of the magnetic fields decreases with depth, indicating that a greater depth results in weaker magnetic anomaly fields. Among the considered fields, the wake magnetic field is the smallest, but the attenuation rate is the fastest, indicating that the wake magnetic field is more affected by depth changes.

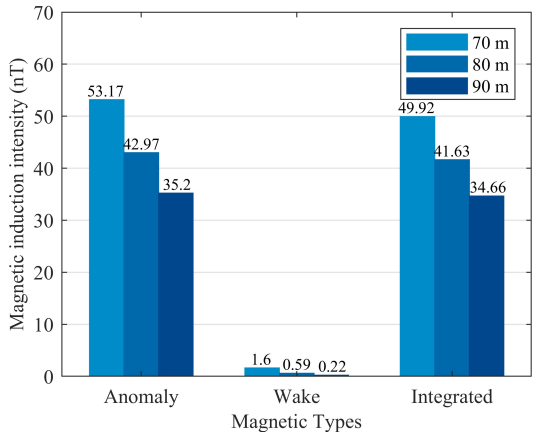

Figure 14. Variation in magnetic induction intensity at different depths.

3.3. Composite Magnetic Field of a Constantly Moving Vehicle in the Presence of Ocean Waves

The parameters of ocean waves and seawater electrical conductivity mainly affect the wake magnetic field and have no significant impact on the magnetic anomaly field. Therefore, in this section, we study the influence of ocean waves on the wake magnetic field under the assumption that the vehicle is moving at a constant speed in a straight line along the x-axis.

3.3.1. Influence of Wind Speed and Direction Changes Under Different Sea States

Sea state codes are categorized based on wind speed and wave height [50], which are closely related to the Beaufort scale. The latter, ranging from Levels 0 to 12, provides a standardized method to gauge wind force based on its visible effects on the sea's surface [51]; when the sea state reaches Code 8 or above, the wind force is already above Level 10 on the Beaufort scale, and ocean navigation is quite dangerous. In this study, we only consider wind speed and wave height values for sea states up to Code 7, as shown in Table 3.

Table 3. Relationship between sea state and Beaufort scale.

Sea State	Beaufort Scale	Wind Speed (kn)	Wave Height (m)
Code 0	Level 0	0	0
Code 1	Level 1	1–3	0–0.1
Code 2	Level 2	4–6	0.1–0.5
Code 3	Level 3 Level 4	7–10 11–16	0.5–0.6 0.6–1.25
Code 4	Level 5	17–21	1.25–2.5
Code 5	Level 6	22–27	2.5–4
Code 6	Level 7	28–33	4–6
Code 7	Level 8 Level 9	34–40 41–47	6–7.5 7.5–10

We selected the maximum wind speeds for sea states corresponding to Codes 1 and 7 and compared the distributions of the wave magnetic field on the detection plane, as shown in Figure 15. An increase in wind speed from 3 kn to 47 kn leads to a noticeable enhancement in the wave magnetic induction intensity. The distribution pattern also shifts from being more localized and less intense to being more widespread and intense, highlighting the significant impact of wind speed on the magnetic field generated by ocean waves.

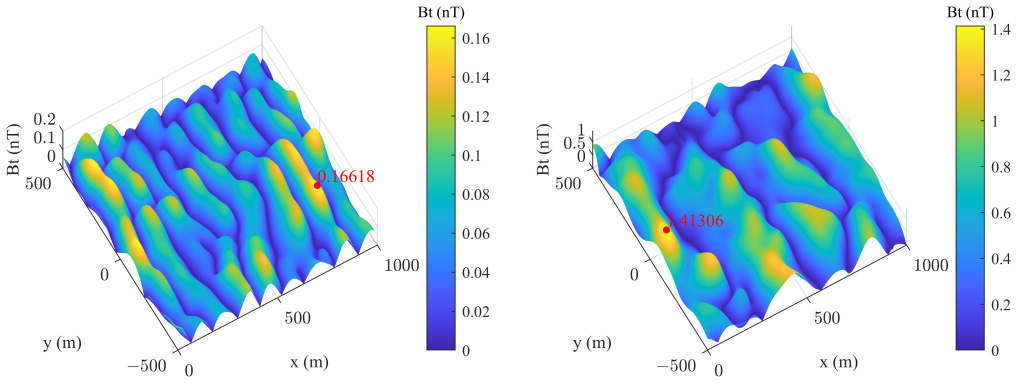

(**a**) (**b**)

Figure 15. Distribution of total magnetic field of ocean waves under different wind speeds. (**a**) Code 1 (3 kn). (**b**) Code 7 (47 kn).

According to Table 3, white waves appear when the sea state reaches Code 4 and wave height exceeds 1 m. To ensure the vehicle's stability and buoyancy, the simulation was conducted under sea state Code 3 (Beaufort Level 3) with a wind speed of 10 kn and a direction of 0°. Figure 16 compares the influence of ocean waves on the wake magnetic field of the vehicle. The presence of ocean waves, as shown in Figure 16b, introduces additional

fluctuations in the wake magnetic vector field components: the z-component exhibits the most significant fluctuations, with a variance standard deviation of 0.4478 nT, followed by the x-component, with a standard deviation of 0.4202 nT, while the y-component shows the smallest fluctuation among the three, with a standard deviation of only 0.1210 nT. Therefore, the influence on the z-component appears to be most pronounced, as indicated by the larger amplitude fluctuations compared with the x- and y-components.

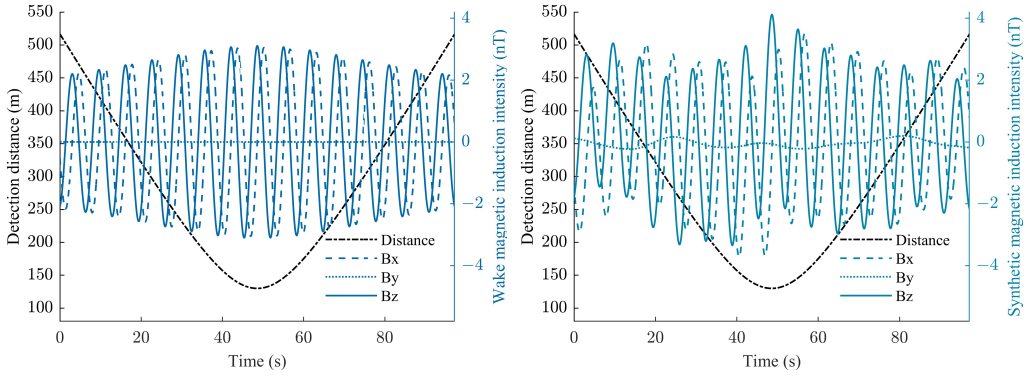

Figure 16. Influence of ocean waves on wake magnetic field. (**a**) With calm sea surface. (**b**) With ocean waves.

The synthetic wake and ocean wave magnetic fields on the detection plane when the wind speed is fixed at 10 kn and the wind direction is set to different angles are superimposed, as shown in Figure 17. As the wind direction changes, the pattern and intensity of the magnetic field distribution also shift, indicating that wind direction significantly influences the magnetic field's spatial characteristics. The wake magnetic field appears to be more intense and concentrated along the wind direction, which is particularly noticeable when the latter is 0°. By comparison, when the wind direction is 45°, the magnetic field shows a decrease in intensity. This suggests that the alignment of the wind direction with the vehicle's wake symmetry axis (refer to Figure 4) increases the intensity of the synthetic magnetic field.

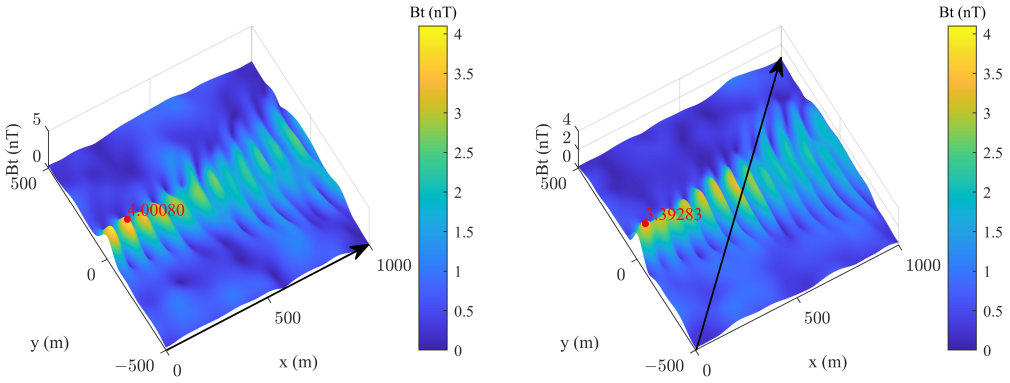

Figure 17. Spatial distribution of synthetic magnetic field for different wind directions. (**a**) Wind direction angle of 0°. (**b**) Wind direction angle of 45°.

3.3.2. Influence of Seawater Electrical Conductivity Changes at Different Geographical Locations

An underwater vehicle's radiated magnetic field is influenced not only by ocean waves but also by seawater electrical conductivity. The distribution map of seawater electrical

conductivity in a specific area (105°–145° E and 0°–30° N) is shown in Figure 18, with the sea depth set to 10 m. The map illustrates that electrical conductivity generally increases as latitude increases, transitioning from lower values (indicated by blue) near the equator to higher values (indicated by red) towards the northern part of the map. Similarly, there is a gradient of conductivity with longitude, with values increasing from west to east. This suggests that the geographical location significantly affects seawater conductivity, which in turn can influence the characteristics of magnetic fields generated by underwater vehicles when sailing in different sea areas.

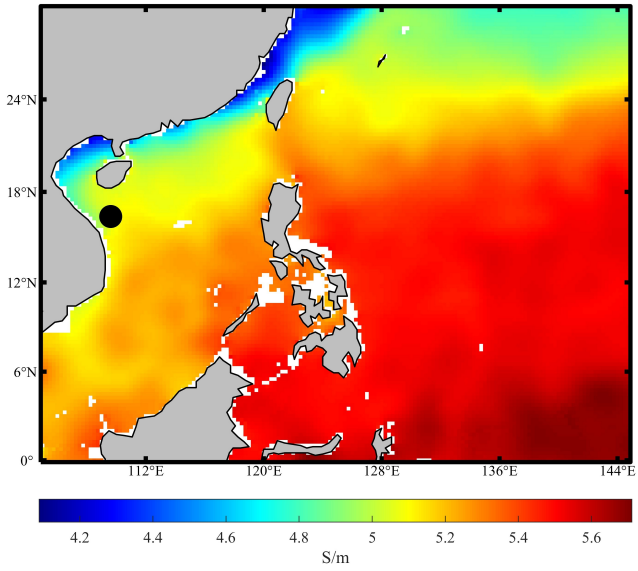

Figure 18. Distribution map of seawater electrical conductivity in a specific area.

The influence of different seawater electrical conductivity values along the detection path on the synthetic wake and ocean wave magnetic fields is compared in Figure 19a. Initially, up to approximately 400 m along the x-axis, the wake magnetic field is dominant, characterized by pronounced magnetic field fluctuations. Beyond this point, the ocean wave magnetic field becomes more prominent as the wake magnetic field diminishes, resulting in reduced amplitude fluctuations. Additionally, an increase in seawater conductivity slightly enhances the wake magnetic field.

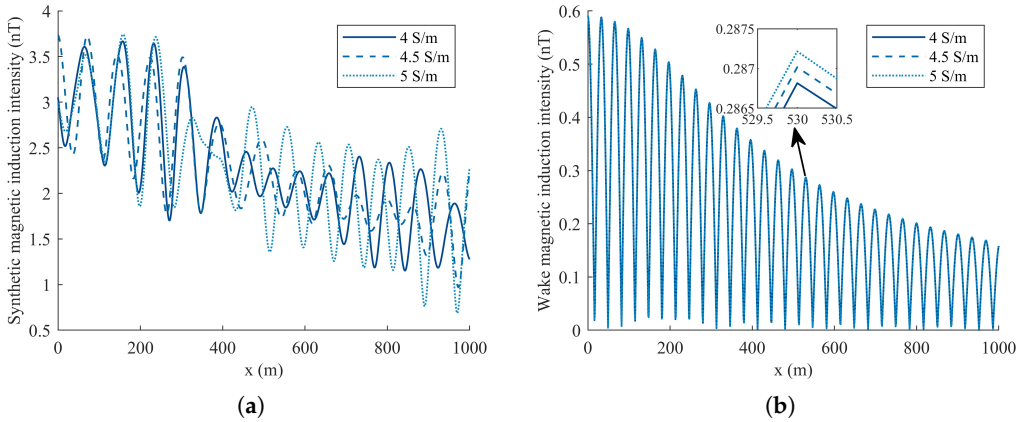

Figure 19. Magnetic fields under different seawater electrical conductivity values along the detection path. (**a**) Synthetic wake and ocean wave magnetic field. (**b**) Wake magnetic field.

Since ocean waves exhibit random motion, the effect of seawater conductivity on their magnetic field does not follow a fixed pattern. In order to study the influence law of electrical conductivity on magnetic fields more accurately, only the wake magnetic field along the detection path is simulated, as shown in Figure 19b. It is evident that the magnetic induction intensity increases with the increase in conductivity. However, the amplitude of the magnetic field fluctuations remains relatively constant across different conductivity levels, indicating that while conductivity influences the overall magnetic induction intensity, it does not significantly alter the characteristic oscillation pattern of the wake magnetic field. A comprehensive comparative analysis of the wake magnetic field's maximum values at different latitudes sampled at 5° intervals from 0°–30° N and longitude fixed at 140° E is detailed in Table 4.

Table 4. Influence of different latitudes on electrical conductivity and wake magnetic field.

Latitude	Conductivity (S/m)	Wake Magnetic Field (nT)
0° N	5.360405	0.563892
5° N	5.263640	0.554419
10° N	5.219599	0.549099
15° N	5.190554	0.538504
20° N	5.178751	0.522960
25° N	4.899721	0.502515
30° N	4.742754	0.477194

Table 4 reveals a consistent pattern: for every 5° increase in latitude, there is a noticeable decrease in conductivity, from 5.360405 S/m to 4.742754 S/m. Concurrently, the wake magnetic field intensity also diminishes, dropping from 0.553892 nT to 0.477194 nT. Therefore, for every 5° increase in latitude, the electrical conductivity decreases by approximately 0.097 S/m, and the wake magnetic field intensity decreases by about 0.014 nT. These data provide a clear quantitative depiction of how both seawater conductivity and the associated wake magnetic field are affected by changes in latitude.

4. Discussion

In Section 2, we presented the magnetic anomaly field of an underwater vehicle and the comprehensive characteristics of the wake magnetic field and, in Section 3, the characteristics of the wave magnetic field and its influence on the wake magnetic field. Therefore, the composite magnetic field measured on the detection plane is obtained by combining the magnetic anomaly, wake, and ocean wave magnetic fields, as shown in Figure 20. Compared with the condition of a calm sea surface, it can be seen that ocean waves slightly alter the shape and distribution of the magnetic field around the vehicle, indicating that wave conditions can modulate the magnetic signatures detected by sensors. Notably, the standard deviation in fluctuations in both the composite and integrated magnetic fields is approximately 0.3741 nT, as illustrated in Figure 20b, indicating that the impact of ocean waves on the magnetic field of the vehicle is relatively minor under sea state Code 3. However, as the sea condition level increases, the influence of waves on the magnetic field generated by the underwater vehicle becomes increasingly significant.

Finally, the effects of vehicle motion and marine environmental parameters on magnetic fields are compared in Table 5, where the arrows indicate the direction of the influence of each parameter on the magnetic field. An upward arrow (↑) indicates a positive correlation between the parameter and the magnetic field intensity, meaning that the intensity generally increases with an increase in the parameter, while a downward arrow (↓) signifies a negative correlation; the arrow combination (↕) signifies that the effect of the parameter on

the magnetic field is not straightforwardly positive or negative, while parameters without arrows have no significant effect on the corresponding magnetic field.

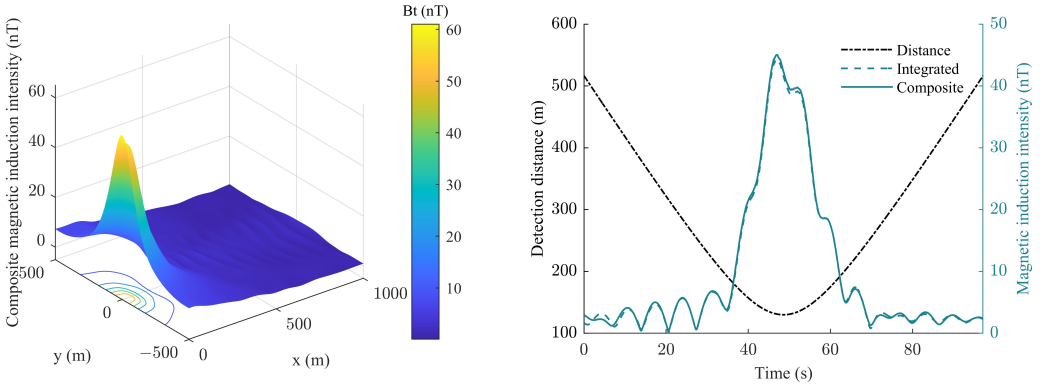

(**a**) (**b**)

Figure 20. Magnetic fields for sea state Code 3. (**a**) Composite magnetic field on detection plane. (**b**) Comparison of composite and integrated magnetic fields at detection point.

Table 5. Influence of vehicle motion and marine environmental parameters on intensity of different magnetic fields.

Parameter	Anomaly	Wake	Wave	Composite
Vehicle course	↕	↕	-	↕
Vehicle speed	-	↑	-	↑
Diving depth	↓	↓	-	↓
Wind direction	-	-	↕	↕
Wind speed	-	-	↑	↑
Electrical conductivity	-	↑	↕	↕

According to Table 5, the specific influence of each parameter on different magnetic fields can be obtained as follows:

1. Magnetic anomaly field: The intensity is influenced by the vehicle's course and diving depth, where a smaller angle between the vehicle's course and the geomagnetic field direction increases the intensity. Marine parameters do not directly affect it;
2. Wake magnetic field: The intensity is significantly affected by the vehicle's speed and diving depth, where higher speeds and smaller depths enhance the wake field's intensity. Additionally, seawater conductivity has a positive impact, reducing the field intensity as conductivity decreases;
3. Ocean wave magnetic field: The intensity of this field is primarily affected by wind speed and direction, where higher wind speeds and specific wind directions that align with the geomagnetic field increase the intensity;
4. Composite magnetic field: The intensity rises with vehicle speed and wind speed but falls with increased diving depth. Additionally, the field is negatively impacted by smaller angles between the vehicle's course and the geomagnetic field, as well as between the wind direction and the geomagnetic field.

5. Conclusions

In conclusion, this study thoroughly examined the composite magnetic fields of underwater vehicles under ocean wave conditions, combining the modeling of the magnetic anomaly field, the wake magnetic field, and the ocean wave magnetic field. Simulation results reveal that a vehicle's motion parameters, including navigation speed, course, and diving depth, significantly affect the distribution of its magnetic field. Additionally,

marine environmental parameters such as wind speed, wind direction, and seawater electrical conductivity play pivotal roles in shaping the composite magnetic field. This study contributes significantly to a profound understanding of the magnetic fields generated by underwater vehicles as they navigate through ocean waves, with the following being unique contributions to this field:

- The exploration of the relationship between vehicle speed and the magnetic anomaly field provides a novel perspective not previously addressed;
- The analysis of how the vehicle's course influences magnetic fields offers novel insights into underwater vehicle dynamics;
- Examining the impact of wind parameters, including wind direction and speed, on ocean wave magnetic fields adds new dimensions to our understanding of the influences of the ocean environment;
- The investigation into the spatiotemporal characteristics of composite magnetic fields under various parameters reveals details previously unstated in other research works.

Our findings underscore the complexity and uniqueness of the magnetic fields under study. Future research will focus on refining the mathematical model by considering the magnetic fields associated with tides and currents in seawater, and exploring additional parameters to better understand the complex interactions between underwater vehicles and the ocean environment.

Author Contributions: Conceptualization, H.W. and X.D.; methodology, H.W.; software, X.D.; validation, H.W.; formal analysis, X.D.; investigation, X.D.; resources, H.W.; data curation, X.D.; writing—original draft preparation, X.D.; writing—review and editing, H.W. and Y.Y.; visualization, X.D.; supervision, H.W.; project administration, H.W. and Y.Y.; funding acquisition, H.W. All authors have read and agreed to the published version of the manuscript.

Funding: This research was funded by the National Natural Science Foundation of China grant number U2341201 and 52271350, the Practice and Innovation Funds for Graduate Students of Northwestern Polytechnical University grant number PF2025003, and the Basic Product Innovation Research Project grant number 1452-0208040.

Data Availability Statement: Data are contained within the article.

Conflicts of Interest: The authors declare no conflicts of interest.

Abbreviations

The following abbreviations are used in this manuscript:

CPA	Closest-Path Approach
FEM	Finite Element Method
IGRF	International Geomagnetic Reference Field
JONSWAP	Joint North Sea Wave Project
MAD	Magnetic Anomaly Detection
WOA	World Ocean Atlas

References

1. Lida, T.; Eleftherios, B.; Panagiotis, P. Magnetic anomaly detection of moving objects. *Phys. B Condens. Matter* **2024**, *676*, 415659. [CrossRef]
2. Liu, Y.F.; Zhang, N.; Shi, Z.S. Research on a matching detection method for magnetic anomaly of underwater targets. *AIP Adv.* **2023**, *13*, 025248. [CrossRef]
3. Zhao, Y.; Zhang, J.H.; Li, J.H.; Liu, S.Q.; Miao, P.X.; Shi, Y.C.; Zhao, Y.M. A brief review of magnetic anomaly detection. *Meas. Sci. Technol.* **2021**, *32*, 042002. [CrossRef]

4. Chen, Z.Y.; Di, W.N.; Chen, R.; Deng, T.Y.; Wang, Y.H.; You, H.R.; Lu, L.; Han, T.; Jiao, J.; Luo, H.S. Modeling and experimental investigation of magnetic anomaly detection using advanced triaxial magnetoelectric sensors. *Sens. Actuator A Phys.* **2022**, *346*, 113806. [CrossRef]
5. Huang, B.; Liu, Z.Y.; Xu, Y.J.; Pan, M.C.; Hu, J.F.; Zhang, Q. Mechanism and evolution of the wake magnetic field generated by underwater vehicles. *Ocean Eng.* **2024**, *303*, 117779. [CrossRef]
6. Wang, H.L.; Ren, Y.D.; Yang, K.D. Electromagnetic field produced by radiation source submerged in non-homogeneous seawater. *Sci. Rep.* **2024**, *14*, 22075. [CrossRef]
7. Chen, Q.; Xuan, Y.M.; Lin, Q.Q.; Han, Y.G.; Wei, K. Evolutions of hydrodynamic and electromagnetic wakes induced by underwater vehicles. *Appl. Ocean Res.* **2023**, *140*, 103750. [CrossRef]
8. Roignant, T.; Josse, N.L.; Boudraa, A.; Szkolnik, J.J.; Penven, P.; Henocq, H. Magnetic Anomaly Detection using Noise-Optimized Orthonormalized Functions on dual magnetometric sensor signals. In Proceedings of the 2024 32nd European Signal Processing Conference (EUSIPCO), Lyon, France, 26–30 August 2024; pp. 2382–2386. [CrossRef]
9. Dai, F.; Chen, J.; Liu, C.; Chen, Z.K.; Peng, D.L. Airborne magnetic anomaly detection based on Bi-stable stochastic resonance system. *Measurement* **2024**, *237*, 115183. [CrossRef]
10. Woloszyn, M.; Tarnawski, J. Minimization of a ship's magnetic signature under external field conditions using a multi-dipole model. *Sci. Rep.* **2024**, *14*, 7864. [CrossRef]
11. Yang, F.; Huang, L. Research on FDTD-PML algorithm for magnetic anomaly analysis and length detection of rebar. In Proceedings of the 2024 3rd International Conference on Artificial Intelligence and Computer Information Technology (AICIT), Yichang, China, 20–22 September 2024; pp. 1–4. [CrossRef]
12. Dong, X.Y.; Wang, H.L. Spatiotemporal variation characteristics of magnetic anomaly field induced by a submerged vessel. In Proceedings of the OCEANS 2025 Brest, Brest, France, 16–19 June 2025; pp. 1–5. [CrossRef]
13. Petruska, A.J.; Abbott, J.J. Optimal permanent-magnet geometries for dipole field approximation. *IEEE Trans. Magn.* **2013**, *49*, 811–819. [CrossRef]
14. Jin, H.H.; Wang, H.; Zhuang, Z.H. A new simple method to design degaussing coils using magnetic dipoles. *J. Mar. Sci. Eng.* **2022**, *10*, 1495. [CrossRef]
15. Wang, M.J.; Liang, X.F.; Yi, H.; Jin, K.F.; Wang, H.D. Magnetic anomaly characteristics analysis of a finite-length submarine cable. *Pure Appl. Geophys.* **2021**, *178*, 4529–4547. [CrossRef]
16. Liu, B.; Cao, Y.; Zhang, H.; Lin, Y.R.; Sun, W.R.; Xu, B. Weak magnetic flux leakage: A possible method for studying pipeline defects located either inside or outside the structures. *NDT E Int.* **2015**, *74*, 81–86. [CrossRef]
17. Nazlibilek, S.; Ege, Y.; Kalender, O. A multi-sensor network for direction finding of moving ferromagnetic objects inside water by magnetic anomaly. *Measurement* **2009**, *42*, 1402–1416. [CrossRef]
18. Shariati, S.K.; Mousavizadegan, S.H. The effect of appendages on the hydrodynamic characteristics of an underwater vehicle near the free surface. *Appl. Ocean Res.* **2017**, *67*, 31–43. [CrossRef]
19. Choi, J.H.; Lee, S.; Ahn, J. Study on the development of the maneuvering mathematical model considering the large angle motion of submarine. *J. Ocean Eng. Technol.* **2023**, *37*, 81–88. [CrossRef]
20. Woloszyn, M.; Tarnawski, J. Magnetic signature reproduction of ferromagnetic ships at arbitrary geographical position, direction and depth using a multi-dipole model. *Sci. Rep.* **2023**, *13*, 14601. [CrossRef]
21. Liu, Y.F.; Zhao, J. Kelvin wake detection from large-scale optical imagery using simulated data trained deep neural network. *Ocean Eng.* **2024**, *297*, 117075. [CrossRef]
22. Kong, D.C.; Yang, Z.T.; Cai, L.; Chai, H.J. An improved wake vortex-based inversion method for submarine maneuvering state. *Comput. Intell. Neurosci.* **2023**, *2023*, 5632128. [CrossRef] [PubMed]
23. Chai, J.; Wang, Z.Y.; Yang, Z.X.; Wang, Z. Investigation of internal wave wakes generated by a submerged body in a stratified flow. *Ocean Eng.* **2022**, *266*, 112840. [CrossRef]
24. Li, L.J.; Zhao, B.B.; Sun, B.K. Surface waves induced by a moving submarine model. *J. Mar. Sci. Appl.* **2023**, *22*, 84–91. [CrossRef]
25. Zilman, G.; Zapolski, A.; Marom, M. On detectability of a ship's kelvin wake in simulated SAR images of rough sea surface. *IEEE Trans. Geosci. Remote Sens.* **2015**, *53*, 609–619. [CrossRef]
26. Fallah, M.A.; Abiri, H. Electromagnetic fields induced by the motion of di-hull bodies in a conducting fluid. *IEEE Trans. Magn.* **2013**, *49*, 5257–5263. [CrossRef]
27. Zhao, S.; Wang, H.L. Research on the characteristics of wake-radiated magnetic fields based on underwater targets. In Proceedings of the 2023 6th International Conference on Information Communication and Signal Processing (ICICSP), Xi'an, China, 23–25 September 2023; pp. 1137–1141. [CrossRef]
28. Phelps, G.; Bracken, R.; Spritzer, J.; White, D. Achieving sub-nanoTesla precision in multirotor UAV aeromagnetic surveys. *J. Appl. Geophys.* **2022**, *206*, 104779. [CrossRef]

29. Fang, C.; Jiao, J.; Ma, J.S.; Lin, D.; Xu, H.Q.; Zhao, X.Y.; Luo, H.S. Significant reduction of equivalent magnetic noise by in-plane series connection in magnetoelectric Metglas/Mn-doped $Pb(Mg_{1/3}Nb_{2/3})O_3$-$PbTiO_3$ laminate composites. *J. Phys. D Appl. Phys.* **2015**, *48*, 465002. [CrossRef]
30. Page, B.R.; Lambert, R.; Mahmoudian, N.; Newby, D.H.; Foley, E.L.; Kornack, T.W. Compact quantum magnetometer system on an agile underwater glider. *Sensors* **2021**, *21*, 1092. [CrossRef]
31. Weaver, J.T. Magnetic variations associated with ocean waves and swell. *J. Geophys. Res.* **1965**, *70*, 1921–1929. [CrossRef]
32. Yaakobi, O.; Zilman, G.; Miloh, T. Detection of the electromagnetic field induced by the wake of a ship moving in a moderate sea state of finite depth. *J. Eng. Math.* **2011**, *70*, 17–27. [CrossRef]
33. Ge, J.Q.; Li, Y.G. Impact of variable seawater conductivity on ocean wave-induced electromagnetic fields simulated with finite difference method. *Front. Earth Sci.* **2023**, *11*, 1194230. [CrossRef]
34. International Geomagnetic Reference Field (IGRF). Available online: https://www.ncei.noaa.gov/products/international-geomagnetic-reference-field (accessed on 20 May 2025).
35. Cronemeyer, D.C. Demagnetization factors for general ellipsoids. *J. Appl. Phys.* **1991**, *70*, 2911–2914. [CrossRef]
36. Zielonacki, K.; Tarnawski, J.; Woloszyn, M. Ship magnetic signature classification using GRU-based Recurrent Neural Networks. *IEEE Access* **2025**, *13*, 59514–59530. [CrossRef]
37. Lu, B.J.; Zhang, X.B. An improved composite ship magnetic field model with ellipsoid and magnetic dipole arrays. *Sci. Rep.* **2024**, *14*, 4070. [CrossRef] [PubMed]
38. Ursell, F. On Kelvin's ship-wave pattern. *J. Fluid Mech.* **1960**, *8*, 418–431. [CrossRef]
39. Madurasinghe, D. Induced electromagnetic fields associated with large ship wakes. *Wave Motion* **1994**, *20*, 283–292. [CrossRef]
40. World Ocean Atlas (WOA). Available online: https://www.ncei.noaa.gov/products/world-ocean-atlas (accessed on 20 May 2025).
41. Madurasinghe, D.; Tuck, E.O. The induced electromagnetic field associated with submerged moving bodies in an unstratified conducting fluid. *IEEE J. Ocean. Eng.* **1994**, *19*, 193–199. [CrossRef]
42. Liang, B.X.; Sun, Z.C.; Liang, S.X.; Cai, L.; Zhao, J.C. Modeling double-peaked spectra by combining two dimensionless JONSWAP models. *Ocean Eng.* **2022**, *266*, 113115. [CrossRef]
43. Hasselmann, K.; Barnett, T.P.; Bouws, E.; Carlson, H.; Cartwright, D.E.; Enke, K.; Ewing, J.A.; Gienapp, H.; Hasselmann, D.E.; Kruseman, P.; et al. Measurements of wind-wave growth and swell decay during the Joint North Sea Wave Project (JONSWAP). *Deut. Hydrogr. Z.* **1973**, *8*, 1–95. Available online: https://www.researchgate.net/publication/256197895 (accessed on 20 May 2025).
44. Chase, J.; Cote, L.J.; Marks, W.; Mehr, E.; Pierson, W.J.; Ronne, F.C.; Stephenson, G.; Vetter, R.C.; Walden, R.G. *The Directional Spectrum of a Wind Generated Sea as Determined from Data Obtained by the Stereo Wave Observation Project*; New York University, College of Engineering, Research Division, Department of Meteorology and Oceanography and Engineering Statistics Group: New York, NY, USA, 1957; pp. 58–81. [CrossRef]
45. Ershkov, S.V.; Rachinskaya, A.; Prosviryakov, E.Y.; Shamin, R.V. On the semi-analytical solutions in hydrodynamics of ideal fluid flows governed by large-scale coherent structures of Spiral-Type. *Symmetry* **2021**, *13*, 2307. [CrossRef]
46. Longuet-Higgins, M.S.; Stern, M.E.; Stommel, H.M. The electrical field induced by ocean currents and waves, with applications to the method of towed electrodes. *Pap. Phys. Oceanogr. Meteorol.* **1954**, *13*, 1–37. [CrossRef]
47. Wang, J.Z.; Jiang, Z.K.; Gao, J.Q.; Zhao, S.X.; Zhai, W.M.; Shen, Y. Frequency characteristics analysis for magnetic anomaly detection. *IEEE Geosci. Remote Sens. Lett.* **2021**, *19*, 8007505. [CrossRef]
48. Lodewyk, K. High strength structural steel in ship and marine engineering structures. *Front. Ocean Eng.* **2022**, *3*, 1–8. [CrossRef]
49. Sarwito, S.; Prananda, J.; Koenhardono, E.S.; Kurniawan, A.W. Study of calculation of degaussing system for reducing magnetic field from submersible vehicle. *Int. J. Mar. Eng. Innov. Res.* **2017**, *1*, 68–75. [CrossRef]
50. Xu, X.O.; Stoffelen, A. Wind and sea state signatures in wind scatterometry: An analysis. *IEEE Geosci. Remote Sens. Mag.* **2025**, *13*, 153–174. [CrossRef]
51. Singleton, F. The Beaufort scale of winds-its relevance, and its use by sailors. *Weather* **2008**, *63*, 37–41. [CrossRef]